Measurements of dendrite tip growth and sidebranching in succinonitrile–acetone alloys

A.J. Melendez, C. Beckermann*

Department of Mechanical and Industrial Engineering, University of Iowa, Iowa City, Iowa 52242, USA

ABSTRACT

Experiments are carried to investigate free dendritic growth of succinonitrile–acetone alloys in an undercooled melt. The measurements include the steady dendrite tip velocity and radius, the non-axisymmetric amplitude coefficient of the fins near the tip, and the envelope width, projection area, and contour length of the sidebranch structure far from the tip. It is found that the measured dendrite tip growth Péclet numbers agree well with the predictions from a stagnant film model that accounts for thermosolutal convection in the melt. The measured tip selection parameter, σ^*, is verified to be independent of the alloy composition, but shows a strong dependence on the imposed undercooling. The universal amplitude coefficient, A_4, is measured to be equal to 0.004, independent of the undercooling, but the early onset of sidebranching prevents its accurate determination for more concentrated alloys. For the self-similar sidebranch structure far from the tip, scaling laws are obtained for the measured geometrical parameters. While melt convection causes some widening of the sidebranch envelope, and the early onset of sidebranching for alloy dendrites results in a 25% upward shift of the envelope width, the projection area and, hence, the mean width of a sidebranching dendrite, as well as its contour length in the sidebranch plane, obey universal power laws that are independent of the convection intensity and the alloy composition.

1. Introduction

Dendrites are a frequently observed growth form during solidification of metal alloys. Understanding the formation of dendritic patterns has been of long standing interest in both the metallurgy and physics communities. Several articles are available that review the state-of-the-art in this field (e.g., Refs. [1–4]). The present study is concerned with steady, free growth of alloy dendrites into an essentially infinite undercooled melt.

Free dendritic growth can be divided into three regimes starting from the tip of the dendrite.

(1) The non-axisymmetric needle-crystal regime, where a dendrite can be represented as a paraboloidal needle with smooth fins developing on four sides (for a crystal with fourfold symmetry); the tip of the needle is characterized by its steady-state growth velocity, V, and radius of curvature, R, while the fins are described, in part, by a fourth-order sinusoidal correction to the parabolic shape with a certain universal amplitude coefficient, A_4; furthermore, a tip selection parameter, $\sigma^* \sim 1/(R^2 V)$, can be defined that depends only on the anisotropy strength of the

crystal, but not on the imposed growth conditions; this side-branch-less regime exists up to a dimensionless distance from the tip of $z/R < 7$–10.

(2) The initial sidebranching regime, where small perturbations start to develop on the fins; these initial sidebranches are well described by linear stability theory; the linear sidebranching regime ends at a dimensional distance from the tip of $z/R < 30$.

(3) The non-linear sidebranching regime, where the sidebranches grow and coarsen simultaneously, but have not yet developed into independent dendrite branches; interestingly, this complex sidebranch structure is still self-similar, in that all geometric parameters can be scaled by the tip radius, R; the non-linear sidebranching regime extends to a dimensionless distance from the tip of $z/R < 1/Pe$, where $Pe \sim VR$ is the tip growth Péclet number; for low melt undercoolings, this regime can be several hundred tip radii long.

The above insights and theories have seen detailed experimental validation mostly for free dendritic growth of pure substances, i.e., thermal dendrites. Very few measurements have been reported for alloy dendrites, whose growth is controlled by both thermal and solutal gradients. As summarized in Ref. [3], a number of researchers have performed experiments to measure the dendrite tip velocity and radius for various transparent alloy systems [5–10]. Of these studies, only the succinonitrile–acetone

* Corresponding author. Tel.: +1 319 335 5681; fax: +1 319 335 5669.
  E-mail address: becker@engineering.uiowa.edu (C. Beckermann).

(SCN–acetone) experiments of Chopra et al. [8] resulted in data over a sufficiently large range of undercoolings and solute concentrations that a detailed comparison with theory is possible. The data show that with increasing solute concentration the tip velocity first increases from the purely thermal value, reaches a maximum at a small but finite acetone concentration, and then decreases as solutal effects start to dominate. The velocity increase is accompanied by a sharp decrease in the tip radius. As shown by Li and Beckermann [11], however, the agreement with the Lipton et al. (LGK) dendrite tip growth model for alloys [12,13] is only approximate, even if melt convection is taken into account. Furthermore, the measured selection parameter, σ^*, shows significant scatter with increasing solute concentration, such that the theory for alloys is still not unambiguously validated [11]. The only study involving alloy dendrites where the universal amplitude coefficient, A_4, was measured is by Dougherty and Lahiri [14], who investigated the tip shape of ammonium chloride dendrites grown from an aqueous solution. They found that $A_4 \approx 0.004$, which is in agreement with the pure SCN measurements of LaCombe et al. [15] and the phase-field simulations for a pure substance of Karma et al. [16]. As far as the two sidebranching regimes are concerned, the lack of experimental data for freely grown alloy dendrites is also disconcerting. Dougherty and coworkers [17–19] measured sidebranching for ammonium bromide, ammonium chloride and pivalic acid (PVA) dendrites grown from various solutions. They found that the mean length of the sidebranches, scaled by the tip radius, is independent of both the growth conditions and the crystalline anisotropy of the material used, up to several hundred dendrite tip radii behind the tip. This finding is in agreement with experimental studies on pure materials, such as SCN, PVA, and xenon [20–27]. However, no power law scaling was observed by Dougherty and coworkers.

In the present study, experiments are performed to investigate free dendritic growth of SCN–acetone alloys. The SCN–acetone system is well suited for the measurement of dendritic growth parameters not only because it is transparent, but also because all relevant thermophysical properties are known accurately and a large body of data is available in the limit of vanishing solute concentration (i.e., pure SCN) [15,23–26,28]. We reexamine in detail the dendrite tip velocity and shape selection for alloys, in order to obtain better validation of the relevant theories and improved understanding of the effects of thermosolutal melt convection. In addition, we measure various geometric integral parameters of the dendrite sidebranches far from the tip, which has not been accomplished for alloy dendrites in the past.

2. Experimental setup and procedures

2.1. Experimental setup

The experimental setup is similar to the one employed in the Isothermal Dendritic Growth Experiments (IDGE) of Glicksman and coworkers [28] and was built by NASA. The apparatus allows for the observation of free dendritic growth of SCN–acetone alloys into an isothermal, undercooled melt. The most important modifications relative to the IDGE are that the concentration of the solute (acetone) can be increased after a set of experiments and that the dendrite can be rotated during the initial growth stages such that the sidebranch planes are always oriented normal to the field of view of two orthogonal cameras.

A schematic of the setup is shown in Fig. 1. The experimental apparatus consists of three major elements: the growth chamber, the isothermal bath, and the optical equipment. The glass growth chamber is situated inside of the isothermal bath and consists of
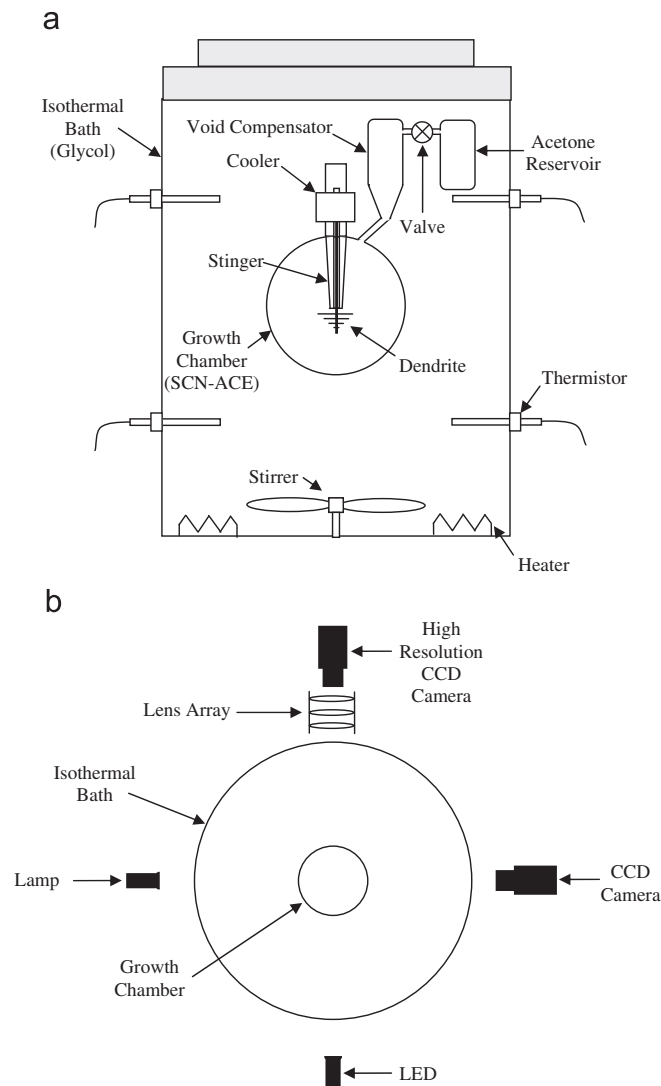

Fig. 1. Schematic of the experimental setup: (a) side view (optical elements omitted); (b) top view.

several components: a spherical compartment, a stinger, a void compensator, a valve, and an acetone reservoir. The spherical compartment contains the SCN–acetone alloy and the stinger from which the growth takes place. Initially, the spherical compartment was filled with 70 cm^3 of ultra-pure (99.998%) SCN and sealed under vacuum. After each set of experiments at a certain solute concentration, acetone was added to the SCN by briefly opening the valve to the acetone reservoir. The solute concentration was determined by measuring the melting point of the alloy (see below). The dendrites are grown from a stinger that consists of a capillary tube extending into the growth chamber. Nucleation is achieved by means of a thermoelectric cooler on the external, closed end of the stinger. Then, the solid propagates through the tube until it emerges at the open end of the stinger inside of the spherical compartment of the growth chamber. Finally, the void compensator, an empty portion of the growth chamber, accommodates expansion of the alloy during melting.

The isothermal bath consists of a temperature controlled cylindrical tank filled with an ethylene glycol–water mixture. This fluid mixture matches the refractive index of liquid SCN. The tank has four optical glass windows through which the dendritic growth is observed. An electrical heater at the bottom of the tank is used to heat the fluid in the bath, while a stirrer ensures temperature

uniformity. Four carefully calibrated thermistors, with a resolution of ± 0.001 K, are installed inside of the tank to monitor the temperature of the fluid. A computer-based data acquisition and control system to which the thermistors and the electrical heater are connected is used to maintain the temperature of the bath at a given set point. The temperature of the fluid in the bath was always uniform to within ± 0.003 K around the set point.

The optical equipment consists of two CCD cameras, a lens array, a lamp, and a LED that are arranged around the isothermal bath as shown in Fig. 1b. One of the cameras is a high-resolution, 15 fps monochrome progressive scan CCD camera. Together with the specially designed long distance microscope lens array, this camera

has a resolution of about 3 μm/pixel. All dendrite shape measurements were performed using images from the high resolution camera. Two examples of such images are shown in Fig. 2. The second CCD camera is a low resolution, color video camera that is oriented at a right angle to the first camera. It was only used to help determine the orientation and growth direction of a dendrite in three-dimensional space, as explained further below. Illumination of the dendrite is supplied by a LED for the high resolution camera and a tungsten lamp for the low resolution camera.

2.2. Experimental procedure

Before each dendritic growth experiment, the bath temperature was set to a temperature slightly above the melting point of the SCN–acetone alloy. This temperature was maintained for up to 12 h in order to allow for complete homogenization of the melt. Then, the bath temperature was lowered to the desired undercooling. After about 1 h, dendritic growth was initiated by briefly turning on the thermoelectric cooler at the closed end of the stinger.

Once the dendrite emerges at the open end of the stinger inside of the growth chamber, it undergoes a period where the growth velocity of the tip continually increases. An example of the evolution of the tip velocity and radius is shown in Fig. 3. At the beginning of this velocity ramp-up period, the growth chamber was rotated such that the dendrite sidebranches were exactly aligned with the cameras (see Fig. 2). After some time, the dendrite tip velocity and radius reach constant values. It is this steady growth period that is of interest in the present study. Eventually, the dendrite starts to interact with the growth chamber walls and the tip velocity and radius start changing again.

Before each set of experiments for a certain alloy composition, the acetone concentration was determined by measuring the melting point of the alloy in-situ. This was done by slowly raising the temperature of the bath, until the last solid melted. The properties of pure SCN and SCN–acetone alloys, including the melting point of pure SCN and the liquidus slope, are provided in Table 1.

Experiments were performed for five different initial acetone concentrations, C_0: 0.0086 mol% (almost pure SCN), 0.1045 mol%, 0.1710 mol%, 0.3065 mol%, and 0.4976 mol%. The uncertainty in the four larger acetone concentrations was estimated to be no more than ± 0.006 mol%. At each solute concentration, experiments were conducted for up to ten different melt undercoolings, ΔT, ranging from 0.1 K to 1 K (± 0.003 K). For each initial solute concentration and undercooling, the experiments were repeated five times. The dendrite tip velocity and shape data presented below always represent mean values of these replications. The reported uncertainties are given by the standard deviation of the individual measurements from the mean.

2.3. Measurement procedures

The dendrite growth velocity and shape measurements were made using the image sequences acquired by the two cameras during an experiment. Before performing any measurements, the images were enhanced by applying a Laplacian of a Gaussian filter [30]. This step results in a more well-defined contour representing the solid–liquid interface.

2.3.1. Growth angle and tip velocity measurements

The coordinates of the dendrite tips in the images from the two cameras were recorded as a function of time and fit to a straight line. The slopes of these two straight lines, m_α and m_β, were then used to determine the growth angles, α and β, in each of the image
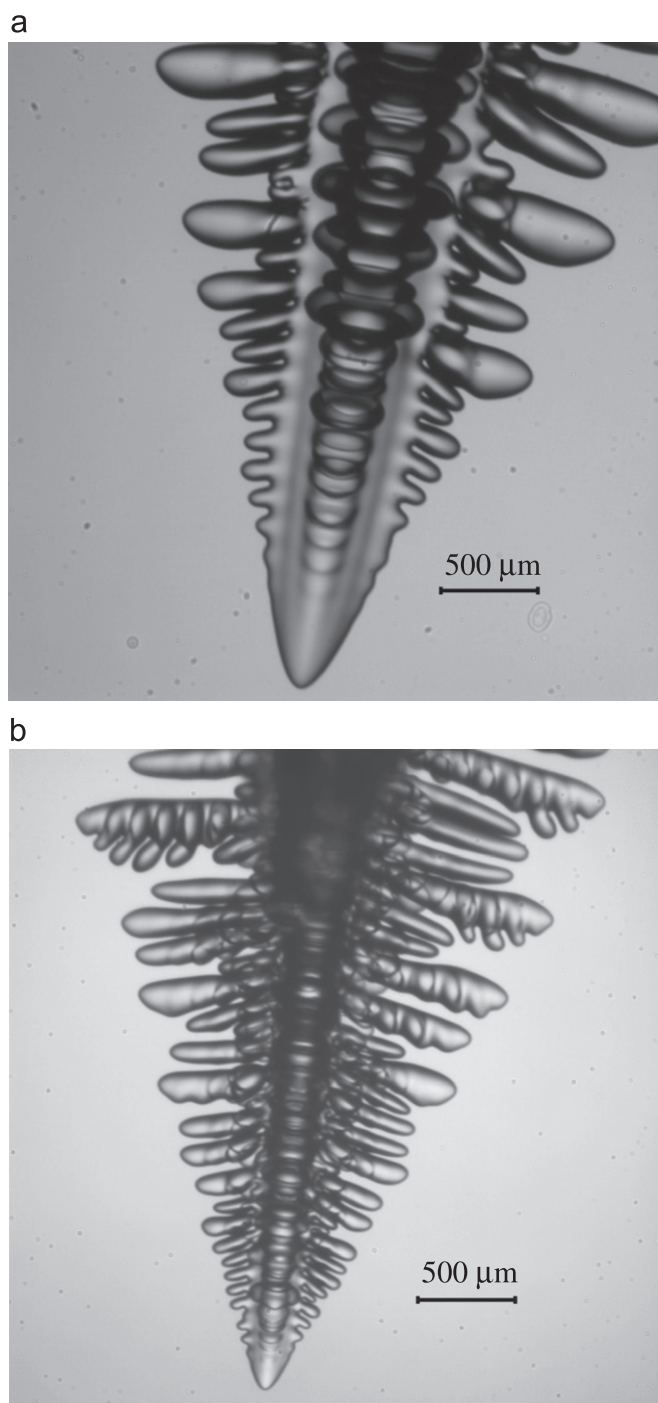
Fig. 2. Typical dendrite images obtained from the high-resolution camera for $\Delta T = 0.200$ K: (a) $C_0 = 0.0086$ mol%; (b) $C_0 = 0.3065$ mol%.
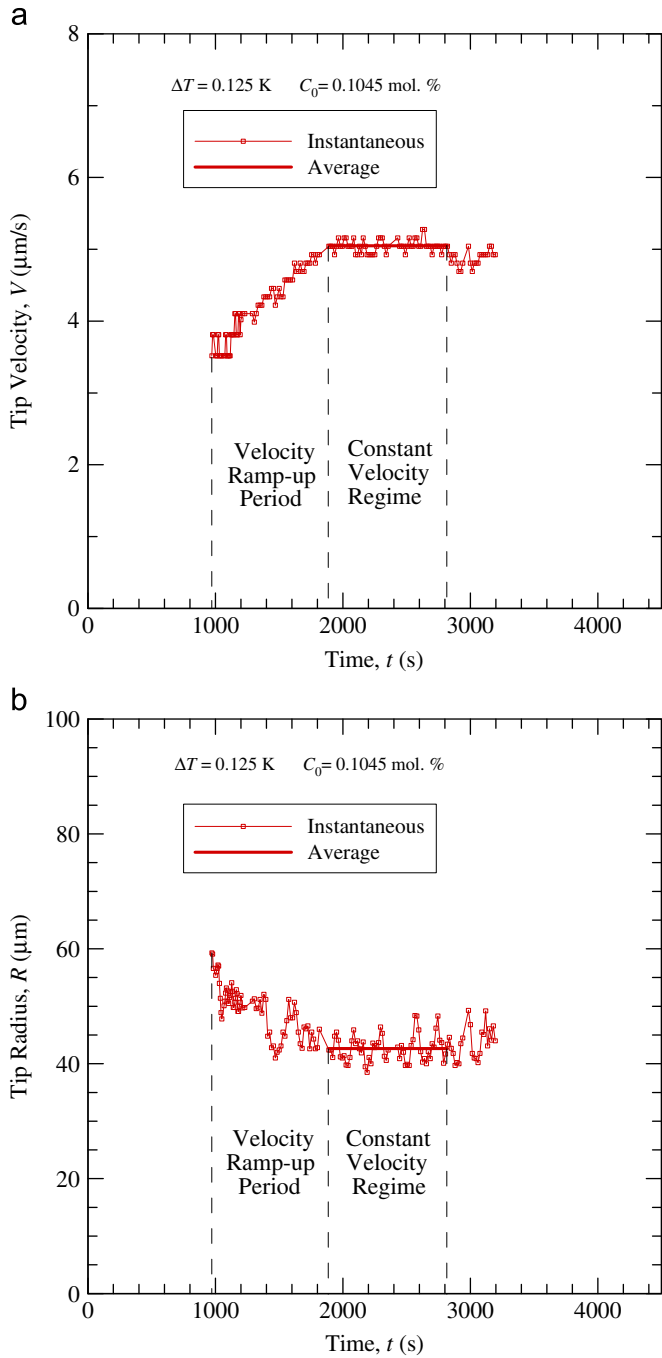
Fig. 3. Example of the variation of the dendrite tip velocity (a) and radius (b) with time ($C_0 = 01045$ mol% , $\Delta T = 0.125$ K).

planes according to

$$\alpha = \tan^{-1}(-1/m_\alpha) \quad \beta = \tan^{-1}(-1/m_\beta) \tag{1}$$

The Eulerian growth angle, θ, which is defined as the angle between the primary dendrite growth axis and the (vertical) gravity vector, is then given by

$$\tan \theta = \sqrt{(\tan \alpha)^2 + (\tan \beta)^2} \tag{2}$$

The dendrite tip growth velocity, V, was measured solely from the images of the high resolution camera. First, the vertical velocity of the tip in the image plane, V_{ver}, was obtained by measuring the downward tip displacement between subsequent images. The time interval between each image was chosen such that approximately

Table 1
Properties of succinonitrile and succinonitrile–acetone alloys [8,11,29].

| Material	Symbol	Property	Value
Succinonitrile	T_m	Melting point	331.231 K
	α	Liquid thermal diffusivity	1.134×10^5 µm²/s
	Γ	Gibbs–Thomson coefficient	6.525×10^{-2} Kµm
	L_f/c_p	Unit supercooling	23.13 K
	d_0	Capillary length	2.821×10^{-3} µm
	$Pr = \nu/\alpha$	Prandtl number	23.1
Succinonitrile– acetone alloy	D	Liquid mass diffusivity	1.27×10^3 µm²/s
	m	Liquidus slope	-2.45 K/mol%
	k	Partition coefficient	0.103 mol%/mol%
	β_T	Thermal expansion coefficient	7.91×10^{-4}/ K at T_m
	β_C	Solutal expansion coefficient	1.68×10^{-3}/ mol% at T_m
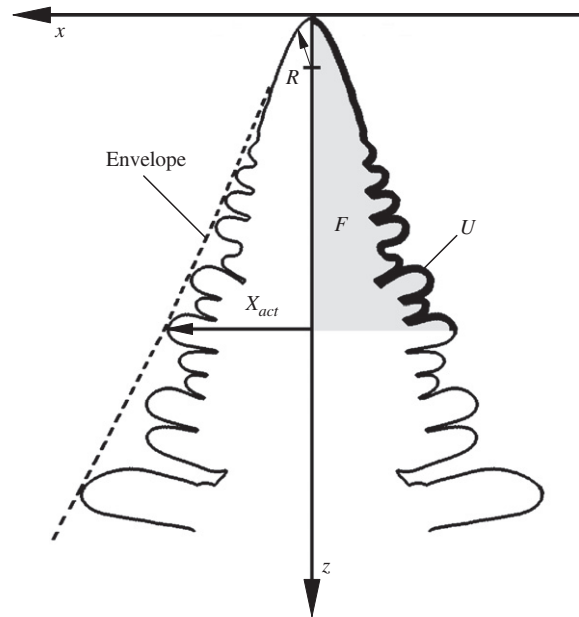
Fig. 4. Schematic of the coordinate system and the various dendrite parameters measured in the present study.

100 images were acquired during each experiment. Then, this velocity was converted to the actual growth velocity using

$$V = V_{ver}/\cos \theta \tag{3}$$

An example of these measurements is shown in Fig. 3a, where the instantaneous growth velocity is plotted as a function of time. It can be seen that there is some scatter in the velocities, which stems from the limited resolution of the camera (3 µm/pixel). In order to obtain a single value of the dendrite tip growth velocity for each experiment, the instantaneous values during the steady growth regime were averaged. This average value is indicated as a bold line in Fig. 3a. The uncertainty in this measurement is approximately given by the standard deviation of the instantaneous velocity values from the mean.

2.3.2. Tip shape measurements

Before performing the tip shape measurements, the dendrite contour in the high-resolution image was rotated and scaled, using the above angle measurements, such that the growth axis lies on the image plane. This scaled dendrite contour then represents the actual dimensions of the dendrite. A coordinate system was assigned to the dendrite contour as shown in Fig. 4. The dendrite tip coincides with the origin of the (x,z) coordinate system and the primary dendrite

axis is aligned with the z axis. Care was taken to ensure that the length scale in the coordinate system correctly reflects the above scaling.

The tip shape measurements were performed using a superposition of ten consecutive images from the steady growth period. By using multiple images, the effects of noise, due to limited image resolution and perturbations in the shape, are much reduced. The coordinates of the scaled dendrite contours from the ten images were regressed to the following fourth-order polynomial

$$z = c_1 x^2 - c_2 x^4 \tag{4}$$

using the so-called robust fitting method [31]. The robust fitting method reduces the influence of outliers on the regression. The fourth-order polynomial fit is motivated by the theory of Ben Amar and Brener [32], who derived the following universal relation for the width of the fins of a non-axisymmetric needle crystal close to the tip

$$\frac{z}{R} = \frac{1}{2}\left(\frac{x}{R}\right)^2 - A_4\left(\frac{x}{R}\right)^4 \tag{5}$$

Hence, the dendrite tip radius of curvature, R, and fourth-order amplitude coefficient, A_4, are given, respectively, by

$$R = \frac{1}{2c_1} \tag{6}$$

$$A_4 = c_2 R^3 \tag{7}$$

When performing the fits, it is important to choose a meaningful fitting range. The dendrite contours were regressed up to a distance, z, of between $2R$ and $11R$ from the tip. Examples of the variations of R and A_4 with the fitting range are shown in Fig. 5. Results are shown for two experiments: (1) almost pure SCN ($C_0 = 0.0086$ mol%) with $\Delta T = 0.1$ K, and (2) a higher solute concentration ($C_0 = 0.1045$ mol%) with $\Delta T = 0.125$ K. Rotated and scaled images of the dendrite contours (near the tip) for these two experiments are shown in Fig. 6. For comparison purposes, the dendrite contours were also fit to a parabola, by setting $A_4 = 0$.

Focusing first on the experiment with almost pure SCN, Fig. 5a shows that the tip radius varies by about 3% for fitting ranges between $6 < z/R < 10$. This insensitivity of the tip radius to the fitting range greatly reduces the uncertainty in this measurement. A parabolic fit gives a larger variation of about 9% over the same fitting ranges, indicating that such a fit is less appropriate for the dendrite tip shape in the plane of the fins. It can also be noticed that the parabolic tip radius is up to 20% larger than the tip radius obtained from the fourth-order polynomial fit. Fig. 5b shows that the amplitude coefficient, A_4, varies from about 0.0052 to 0.0043 for the fitting range increasing from $z/R = 6$ to 10. A similar sensitivity of A_4 to the fitting range and was also observed in the phase-field simulations for a pure substance of Karma at al. [16]. Choosing a larger fitting range, in order to overcome this sensitivity, is prevented by the fourth-order polynomial fit strongly diverging from the dendrite shape for z/R greater than about 11 to 14, depending on the value of A_4. This is illustrated by the (green) dotted lines in Fig. 6. Furthermore, as can be seen from the dendrite image in Fig. 6a, the first sidebranches start to appear at about $z/R = 10$. The fin amplitude coefficient A_4 has little meaning in the presence of significant sidebranching. Therefore, a fitting range of $z/R = 10$ was chosen for all of the present tip shape measurements.

For the higher solute concentration ($C_0 = 0.1045$ mol%), Fig. 5a shows a similar insensitivity of the tip radius to the fitting range. The tip radius varies by only 2% for fitting ranges between $6 < z/R < 10$ (again, the parabolic fit is less appropriate). This insensitivity is remarkable, because in all experiments with finite solute
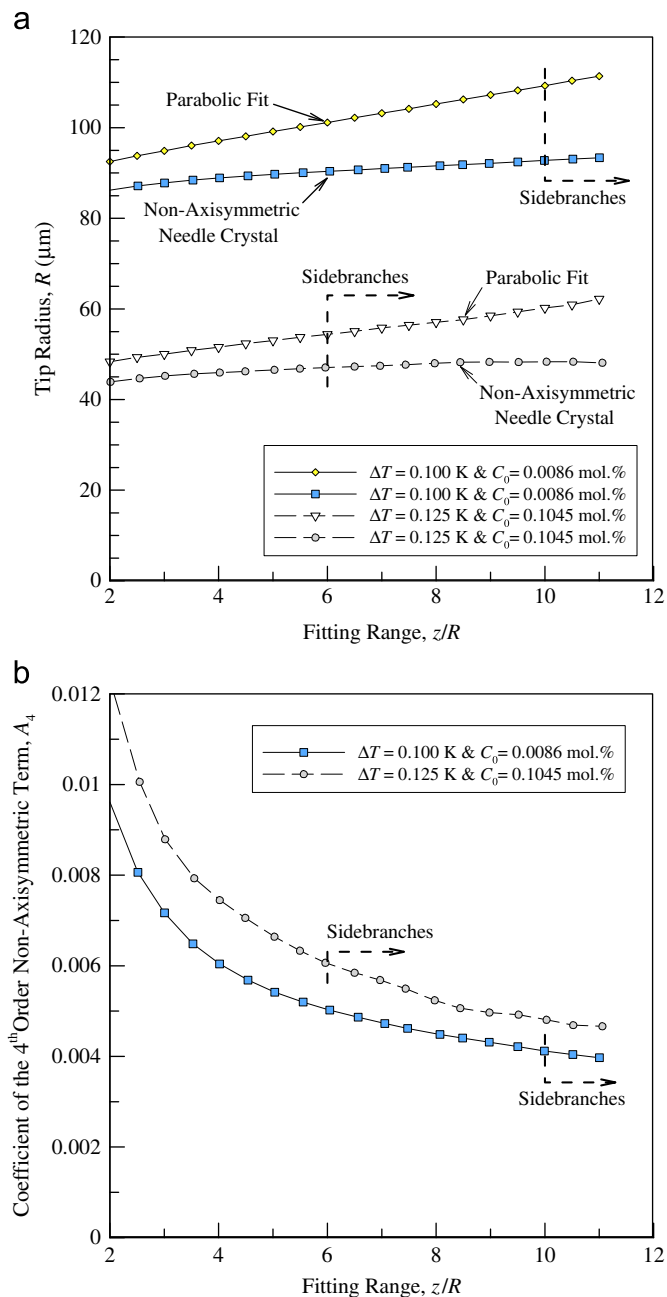

Fig. 5. Variation of the tip radius (a) and the fourth-order amplitude coefficient (b) with the fitting range for two experiments.

concentrations ($C_0 > 0.1$ mol%), small sidebranches start to appear at about $z/R = 6$, as opposed to $z/R = 10$ for almost pure SCN. Fitting the tip shape to a fourth-order polynomial even in the presence of sidebranches (for $6 < z/R < 10$) is made possible in the present study by the use of a superposition of ten consecutive dendrite images and the robust fitting method. However, a problem is encountered when trying to determine A_4 for the alloy experiments. For the experiment with $C_0 = 0.1045$ mol%, Fig. 5b shows the same large variation of A_4 with the fitting range as for almost pure SCN, although the values are slightly higher. Using A_4 values for fitting ranges of $z/R < 6$ is inappropriate, because the fitted dendrite shape is, within the measurement uncertainty, indistinguishable from a parabolic fit ($A_4 = 0$). This is demonstrated by the green and red dotted lines in Fig. 6. On the other hand, using a fitting range of $z/R > 6$ is questionable because of the presence of sidebranches in the alloy experiments. It could
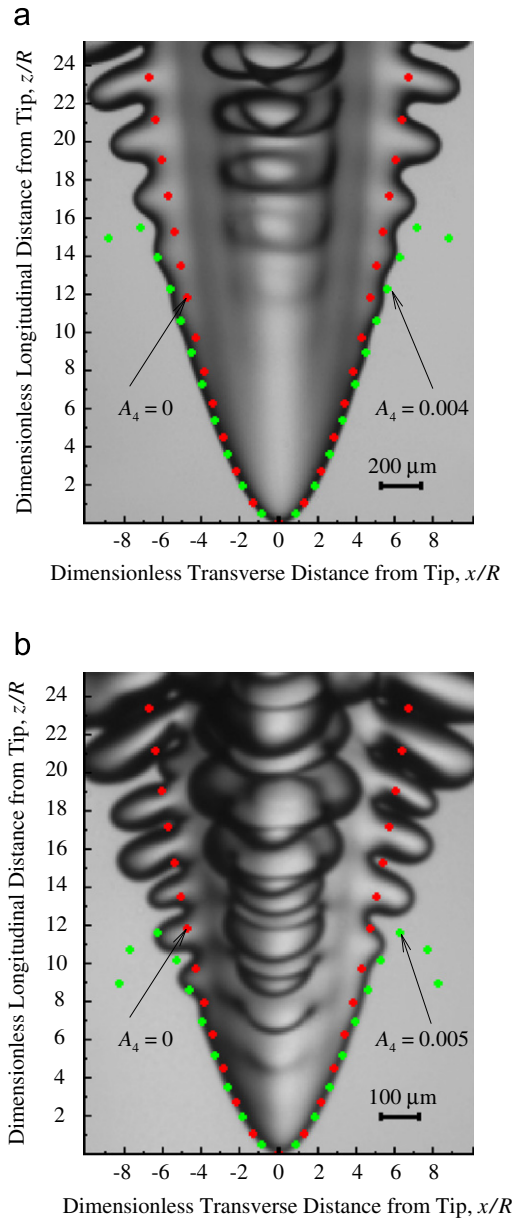
a

b

Fig. 6. Scaled and rotated dendrite images showing the fitting of the dendrite tip shape: (a) almost pure SCN (C_0=0.0086 mol%, ΔT=0.100 K); (b) SCN–acetone alloy (C_0=0.1045 mol%, ΔT=0.125 K).

be argued that the initial sidebranching instability is small enough that the use of the mean dendrite shape from ten images allows for a fitting range of z/R up to about 10 (see Fig. 6b), but the resulting uncertainty would be large. Hence, due to the presence of "early" sidebranching, data for the amplitude coefficient A_4 for alloys are not reported in the present study. Nonetheless, it may be surmised from Fig. 5b that at z/R=10, the value of A_4 for alloys is close (within 15%) to the one for almost pure SCN.

2.3.3. Sidebranching measurements

The overall extent of the sidebranches of a dendrite can be described by the width of the dendrite envelope in the sidebranch plane, $X_{act}(z)$, as illustrated in Fig. 4. The dendrite envelope is a smooth curve connecting the tips of the actively growing sidebranches. A sidebranch is defined as active when it is longer than the next active sidebranch closer to the tip. The envelope width is then obtained by measuring the length (from the dendrite axis) of the actively growing sidebranches. Li and Beckermann [23]

measured the envelope width for pure SCN dendrites grown in microgravity and found that in the self-similar regime, $X_{act}(z)$ follows a simple power law with distance from the tip. This power law is independent of undercooling when all lengths are normalized by the dendrite tip radius. Such a power law is also measured in the present study of SCN–acetone dendrites grown on earth, in order to examine if the same power law holds for alloys and in the presence of convection.

Dendrite envelopes, as defined here, have been found to be useful in a variety of averaged models of solidification grain structure development [34–39]. This is the case because their evolution can be described by dendrite tip growth models. These growth models only apply to actively growing tips. The shorter, inactive sidebranches grow much slower or are even shrinking (see Fig. 2), so their length is no longer related to dendritic growth. Steinbach et al. [36], in particular, demonstrate how the envelope shape measured by Li and Beckermann [23] can be used to validate a so-called mesoscopic model of dendritic growth that predicts the envelope evolution for an entire three-dimensional dendrite. From this point of view, it is unclear why Dougherty and coworkers [17–19], Corrigan et al. [24], and Giummarra et al. [26] included the inactive sidebranches in their sidebranch envelope measurements. Corrigan et al. [24] claim that by including all sidebranches (active and inactive), a "true" sidebranch envelope is obtained, because the shorter sidebranches still affect the "thermal field and the process in general". While this may be true for the region between the sidebranches, which is more or less isothermal, the inactive sidebranches do not affect the tip growth of the active sidebranches, as shown by Steinbach et al. [36]. Note from Fig. 2 that the length of most inactive sidebranches is a small fraction of the length of a neighboring active sidebranch. If these short and shrinking sidebranches were included in the envelope measurements, the envelope motion could no longer be described by dendrite tip growth models. Hence, despite the inability to compare our envelope measurements directly to those of other researchers, the envelope definition involving only active sidebranches is retained here.

It is also desirable to measure the mean width of the sidebranch structure of a dendrite, including not only the peaks (i.e., the sidebranch tips) but also the valleys close to the primary stem (see Fig. 2). The motivation behind such a measurement is the theory of Brener [33] for the shape of a thermal non-axisymmetric needle crystal far from the tip ($z/R > 1$), where the heat flow along the dendrite axis can be neglected. According to this theory, the width of the four fins is given by the following power law

$$\frac{z}{R} = \frac{3}{5}\left(\frac{x}{R}\right)^{5/3} \tag{8}$$

The three-dimensional phase-field simulations of Karma et al. [16] showed that for thermal dendrites without sidebranches, this power law fits the computed fin shape up to distances from the tip of at least z/R=20. However, as noted in the previous subsection and seen in Fig. 6, sidebranches start to develop on the fins at $z/R \approx 10$ for pure SCN and $z/R \approx 6$ for SCN–acetone alloys. Then, it is more appropriate to average the sidebranch structure and compare the mean width of a dendrite in the sidebranch plane to Brener's power law. Due to the complex morphology of the sidebranches, it is difficult to measure such a mean dendrite width. It is much easier to measure the variation of the projection area, F, of a dendrite in the sidebranch plane with distance from the tip. The definition of the projection area is illustrated in Fig. 4. Brener's prediction for the projection area, obtained by integrating Eq. (8), is given by

$$\frac{F}{R^2} = 0.85\left(\frac{z}{R}\right)^{3/5+1} \tag{9}$$

Li and Beckermann [25] found that for pure SCN dendrites grown in microgravity, the above power law holds to within

measurement uncertainty up to $z/R = 30$, thus verifying Brener's power law, Eq. (8). Recall that $z/R = 30$ marks the end of the linear sidebranching regime. At larger distances from the tip, in the non-linear sidebranching regime, Li and Beckermann [25] found that the projection area still follows a power law like Eq. (9), but the pre-factor and exponent changed, respectively, to 0.58 and 1.72 (instead of $3/5 + 1 = 1.6$). In the present study, the variation of the projection area is measured for the first time for alloy dendrites, in order to determine if such dendrites obey the same power law as purely thermal dendrites. In addition, since the present experiments are performed in earth's gravitational field, the effect of melt convection can be examined.

The complex nature of the interfacial morphology in the non-linear sidebranching regime ($z/R > 30$) can be described, in part, by the contour length, U, of the solid–liquid interface in the sidebranch plane. This quantity is also illustrated in Fig. 4. The contour length can be viewed as a measure of the fineness of the sidebranch structure, as governed by the simultaneous growth and coarsening processes occurring far from the dendrite tip. Li and Beckermann [23,25] found that, when scaled by the dendrite tip radius, the contour length of a purely thermal dendrite obeys a universal power law for its variation with distance from the tip in the non-linear sidebranching regime. Such measurements are repeated here for alloy dendrites using the scaled and rotated high-resolution images acquired in the present experiments.

3. Review of free dendrite tip growth models for alloys

Before presenting the experimental results, it is useful to briefly review the Lipton–Glicksman–Kurz (LGK) [12,13] and Li–Beckermann (LB) [11] dendrite tip growth models for alloys, since the present measurements of the tip velocity and radius will be extensively compared to these theories. The LGK model is valid for free dendritic growth of alloys at low undercoolings, but assumes purely diffusive heat and solute transport in the melt. The LB model is a simple modification to the LGK model to account for thermo-solutal natural convection in the melt.

Neglecting kinetic effects, the total imposed undercooling, ΔT, is given by the sum of the thermal, ΔT_T, solutal, ΔT_C, and curvature, ΔT_R, undercoolings as

$$\Delta T = \Delta T_T + \Delta T_C + \Delta T_R \tag{10}$$

Dimensionless thermal and solutal undercoolings can be defined, respectively, as

$$\Omega_T = \frac{T_t^* - T_0}{L_f/c_p} \quad \text{and} \quad \Omega_C = \frac{C_t^* - C_0}{C_t^*(1-k)} \tag{11}$$

where L_f is the latent heat of fusion, c_p is the liquid specific heat, k is the partition coefficient, T_0 and C_0 are the initial or far-field melt temperature and solute concentration, respectively, and T_t^* and C_t^* are the temperature and solute concentration in the liquid at the dendrite tip, respectively. Using the Gibbs–Thomson relation for the curvature undercooling, Eq. (10) can be rewritten as

$$\Delta T = \left(\frac{L_f}{c_p}\right)\Omega_T + \frac{k\Delta T_0 \Omega_C}{1-(1-k)\Omega_C} + \frac{2\Gamma}{R} \tag{12}$$

where Γ is the Gibbs–Thomson coefficient and $\Delta T_0 = mC_0(1-1/k)$ is the equilibrium freezing temperature range of the alloy, in which m is the liquidus slope.

The dimensionless undercoolings are obtained as a function of the growth Péclet numbers from an appropriate transport theory. The thermal and solutal growth Péclet numbers are defined, respectively, as $Pe_T = VR/2\alpha$ and $Pe_C = VR/2D$, where α and D are the thermal and mass diffusivities, respectively, of the liquid. In the LGK model, the Ivantsov solution [40] for steady diffusion

around a growing paraboloid of revolution is used. In the LB model for convection, the stagnant film solution of Cantor and Vogel [41] is employed, in which the dimensionless thermal and solutal undercoolings are calculated from

$$\Omega_T = Pe_T \exp(Pe_T)\{E_I(Pe_T) - E_I[Pe_T(1+2\delta_T/R)]\} \tag{13}$$

$$\Omega_C = Pe_C \exp(Pe_C)\{E_I(Pe_C) - E_I[Pe_C(1+2\delta_C/R)]\} \tag{14}$$

where E_I is the exponential integral function and δ_T and δ_C are the thermal and solutal boundary layer thicknesses, respectively. Note that for $\delta_T/R \to \infty$ and $\delta_C/R \to \infty$, Eqs. (13) and (14) reduce to the Ivantsov solution. In the LB model, the boundary layer thicknesses are obtained from the following laminar thermoso-lutal natural convection correlations

$$\frac{\delta_T}{R} = 2.2\,(Ra_T)^{-1/4}\left(1+\frac{N}{\sqrt{Le}}\right)^{-1/4} \tag{15}$$

$$\frac{\delta_C}{R} = 2.2\,(Ra_C)^{-1/4}\left(1+\frac{\sqrt{Le}}{N}\right)^{-1/4} \tag{16}$$

where $Le = \alpha/D$ is the Lewis number. The buoyancy parameter, N, the thermal Rayleigh number, Ra_T, and the solutal Rayleigh number, Ra_C, are defined, respectively, as

$$N = \frac{\beta_C(C_t^* - C_0)}{\beta_T(T_t^* - T_0)} \tag{17}$$

$$Ra_T = \frac{\beta_T g(T_t^* - T_0)R^3}{\alpha v} \tag{18}$$

$$Ra_C = \frac{\beta_C g(C_t^* - C_0)R^3}{Dv} \tag{19}$$

where β_C is the solutal expansion coefficient, β_T is the thermal expansion coefficient, and v is the kinematic viscosity of the liquid, while g is the gravitational acceleration. The constant 2.2 in Eqs. (15) and (16) was determined by calibrating the LB theory against the terrestrial dendritic growth experiments for pure SCN by Koss et al. [28]. In those experiments the dendrites grew approximately, but not exactly in a downward direction (in the direction of the gravity vector). Since in natural convection the heat or solute transport depends strongly on the orientation of the body with respect to gravity, the constant 2.2 can be expected to be different for other growth directions.

The LGK and LB models use the same dendrite tip shape selection criterion, which for free growth of alloy dendrites can be written as [1]

$$\sigma^* = \frac{d_0}{R}\left[2Pe_C\left(\frac{k\Delta T_0/(L_f/c_p)}{1-(1-k)\Omega_C}\right)+Pe_T\right]^{-1} \tag{20}$$

where $d_0 = \Gamma/(L_f/c_p)$ is the capillary length. According to Trivedi and Kurz [1], the selection parameter, σ^*, is independent of the undercooling and the alloy composition.

4. Results and discussions

4.1. Dendrite tip growth velocity and radius

The measured dendrite tip growth velocities and radii are plotted as a function of the undercooling in Figs. 7 and 8, respectively, as solid circles. The data for each of the five initial acetone concentrations are presented in separate sub-figures. The measurements are compared to both the LGK (dashed lines) and LB (solid lines) models. The lines represent the model predictions for $\sigma^* = 0.02$. This value of the selection parameter represents an approximate mean of the σ^* values measured at low undercoolings
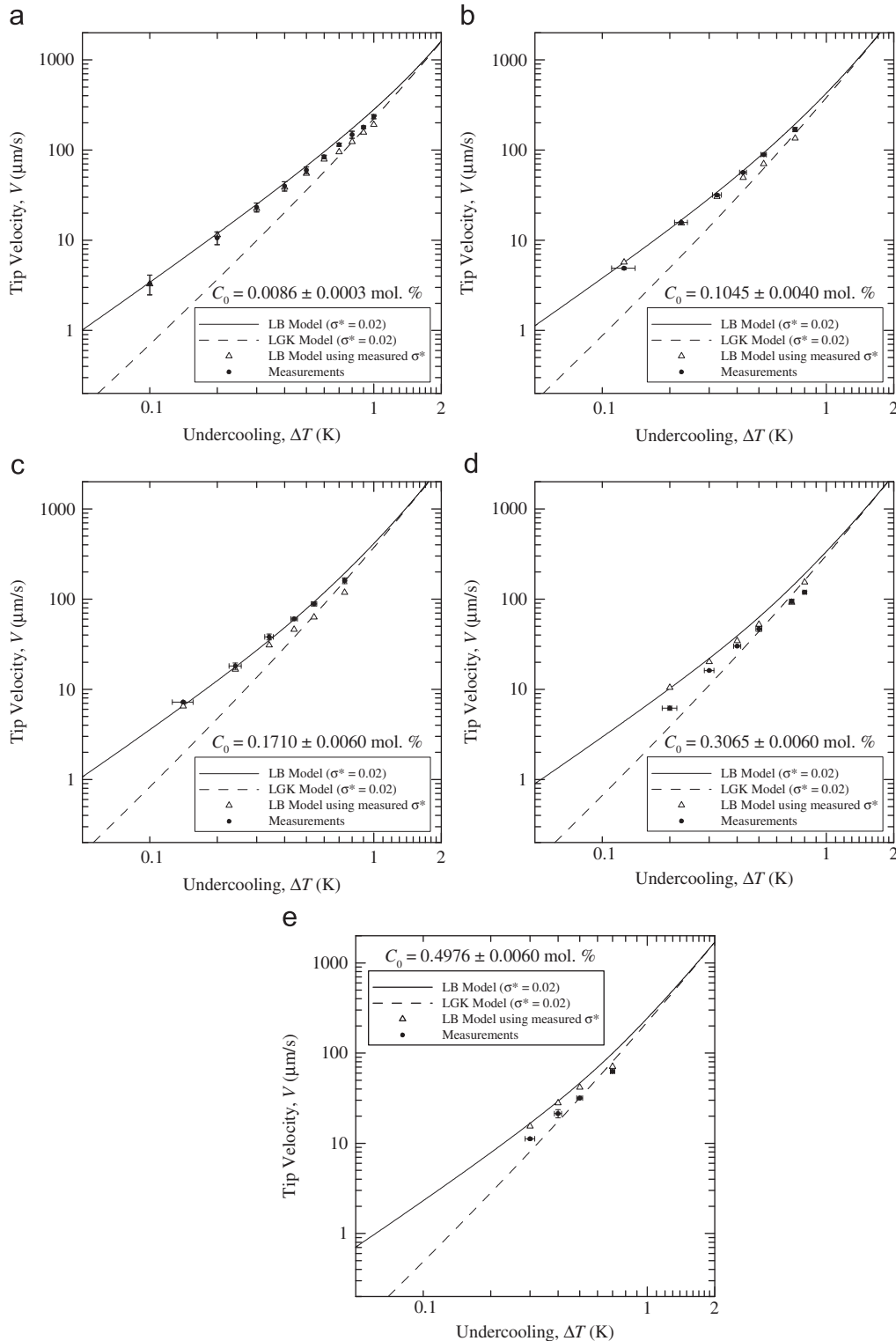
Fig. 7. Comparison of measured and predicted dendrite tip velocities as a function of undercooling: $C_0 =$ (a) 0.0086, (b) 0.1045, (c) 0.1710, (d) 0.3065, (e) 0.4976 mol%.

(see below). The open triangles represent the predictions of the LB model using the σ^* that was actually measured for a particular undercooling and alloy composition.

Figs. 7 and 8 show that, as expected, the tip velocity increases and the tip radius decreases with increasing undercooling. Overall, excellent agreement is obtained between the measurements and the predictions of the LB model, which accounts for melt convection. At low undercoolings, large discrepancies with the LGK model can be observed, indicating that melt convection plays an important role. In fact, at an undercooling of 0.1 K, the measured dendrite tip velocities are up to a factor of four higher than the predictions from the diffusion theory. As the undercooling increases to about 1 K, the lines representing the LGK and LB models merge, indicating that melt convection plays almost no role. While this behavior has been previously reported for dendritic growth of pure substances [28], the present measurements indicate that it is also
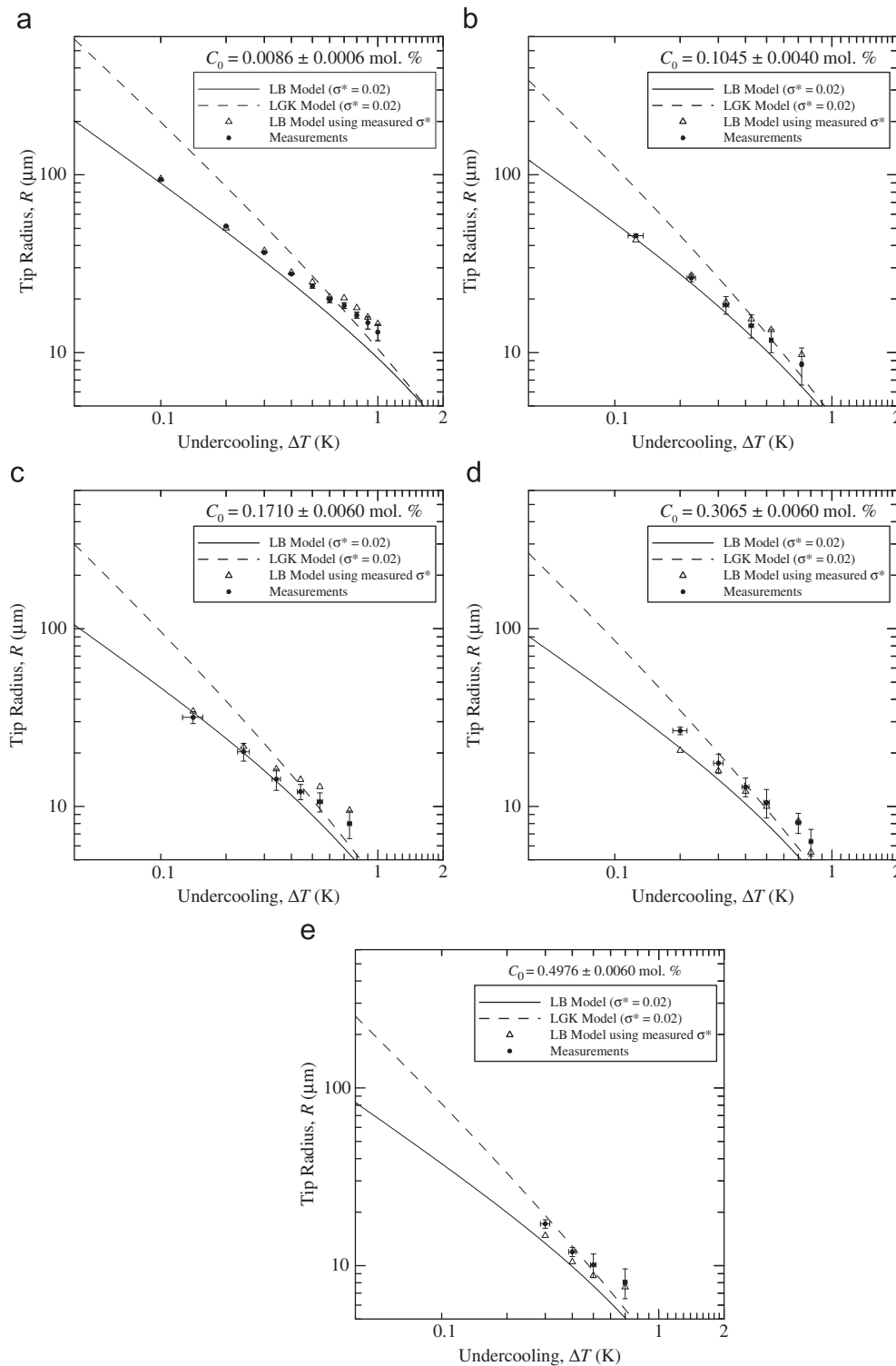
Fig. 8. Comparison of measured and predicted dendrite tip radii as a function of undercooling: C_0=(a) 0.0086, (b) 0.1045, (c) 0.1710, (d) 0.3065, (e) 0.4976 mol%.

true for alloy dendrites. Some discrepancies between the dendrite tip velocity and radius measurements and LB model predictions can be observed at the two highest solute concentrations (C_0=0.3065 mol% and 0.4976 mol%). As discussed below, these differences are likely due to inaccuracies in the LB model for convection.

In Figs. 9a and b, the measured and predicted dendrite tip growth velocities and radii are plotted, respectively, as a function of the initial solute concentration, C_0. The two plots are for an undercooling equal to 0.5 K, but some of the measurements are at

slightly higher undercoolings. Fig. 9a shows that with increasing solute concentration, the tip velocity first sharply increases, reaches a maximum around C_0=0.1 mol%, and then gradually decreases. Overall, the tip velocity measurements are in reasonable agreement with the LB model, although at higher solute concentrations some disagreement can be observed. The LGK model, which neglects melt convection, does generally not provide good agreement, especially at low solute concentrations. The tip radii, shown in Fig. 9b, decrease sharply with increasing solute
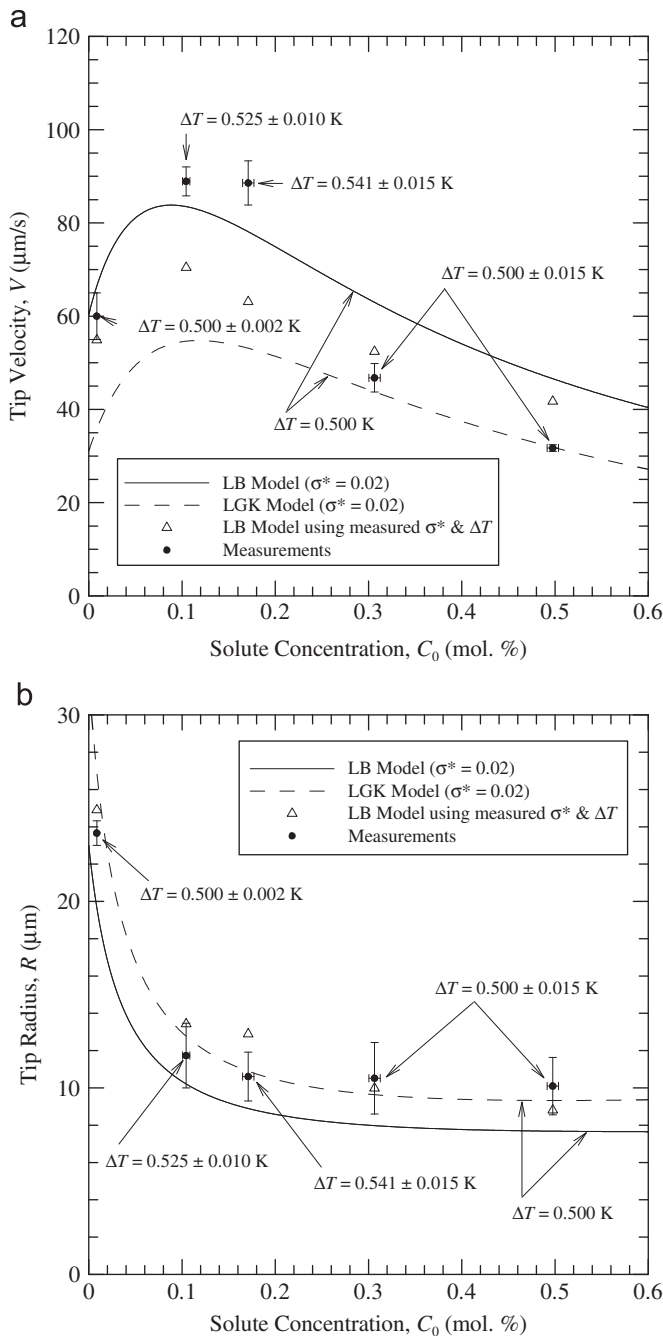
Fig. 9. Comparison of measured and predicted tip velocities (a) and radii (b) as a function of solute concentration for undercoolings near 0.5 K.

concentration and until they reach an approximately constant value for $C_0 \geq 0.1$ mol%. The tip radius measurements are also in much better agreement with the LB model than with the LGK model.

4.2. Dendrite tip Péclet number

The transport part of the dendrite tip growth models can be better examined by comparing the measured and predicted growth Péclet numbers. This is because the Péclet number depends only weakly on the tip selection parameter. In the absence of convection, the Péclet number can be calculated directly from the knowledge of the undercooling (i.e., through the Ivantsov solution), and no knowledge of σ^* is necessary. In the presence of convection, a weak

dependence on σ^* exists due to the tip radius appearing independently in the expressions for the boundary layer thicknesses [see Eqs. (15)–(19)]. Measured Péclet numbers are simply obtained by substituting a measured dendrite tip velocity and radius pair into the expression $Pe_T = VR/2\alpha$. Note that the solutal Péclet number is related to the thermal Péclet number by a constant multiplier equal to the Lewis number, $Le \approx 90$.

Fig. 10 shows the measured and predicted thermal Péclet numbers as a function of the undercooling for each of the five initial solute concentrations. The measurements and the predictions show the expected increase of the Péclet number with increasing undercooling. The excellent agreement of the measured Péclet numbers with the LB model, together with the poor agreement with the LGK model, indicates that the convection correlations used in the LB model are generally accurate and appropriate for the present experiments. Note that the differences between the predictions of the LB model using $\sigma^*=0.02$ (solid line) and using the measured σ^* (open triangles) are indeed negligibly small.

The agreement is somewhat less favorable at the two highest solute concentrations (see Figs. 10d and e). This may be attributed to the fact that the LB model was calibrated by matching its predictions with data that are available for terrestrial growth of pure SCN dendrites only [11]. In the present experiments with almost pure SCN ($C_0=0.0086$ mol%), as well as in the experiments with the next two higher solute concentrations ($C_0=0.1045$ mol% and 0.1710 mol%), the dendrites grew approximately downward, with an average Eulerian angle of 15°. This can be seen from the histogram of the measured Eulerian angles shown in Fig. 11. Since for these three initial compositions the measured and predicted Péclet numbers agree almost perfectly (especially at low undercoolings where convection effects are most important), it can be said that the convection correlations in the LB model, given by Eqs. (15) and (16), are well calibrated for growth angles of $15° \pm 5°$. However for the experiments with the two highest initial solute concentrations ($C_0=0.3065$ mol% and 0.4976 mol%), Fig. 11 shows that the average Eulerian growth angle was significantly higher, about 21°. In fact, 80% of the dendrites grew with an Eulerian angle greater than 15°. Based on the results for the angle dependency of the dendrite growth velocity presented in Badillo et al. [37], the less favorable agreement between the measured and predicted Péclet numbers for the two highest solute concentrations can readily be attributed to the observed differences in the growth angle with respect to gravity. Including the growth angle dependency in the LB model is outside the scope of the present study.

4.3. Dendrite tip selection parameter and amplitude coefficient

The dendrite tip selection parameters measured in the present experiments are plotted in Fig. 12 as a function of the undercooling. A measured σ^* is obtained by substituting a measured dendrite tip growth velocity and radius pair into Eq. (20). However, the dimensionless solutal undercooling, Ω_C, in Eq. (20) needs to be calculated, since the solute concentration at the tip, C_t^*, is not measured. This is accomplished using Eq. (14) with measured V and R data. The uncertainty bar shown for each σ^* in Fig. 12 represents the standard deviation of the five repeats of each experiment, and includes the uncertainties in the measured dendrite tip growth velocity and radius.

Fig. 12 shows that σ^* decreases from a mean value of about 0.02 at undercoolings close to 0.1 K to about 0.012 at undercoolings approaching 1.0 K. Similar values for σ^* and a similar dependency on the undercooling have been measured previously by Glicksman and coworkers for pure SCN [28] and, more recently, for pure PVA [42]. The present experiments show that within the measurement uncertainty there is no discernable effect of the alloy composition on the selection parameter, i.e., σ^* is not a function of C_0. This result is
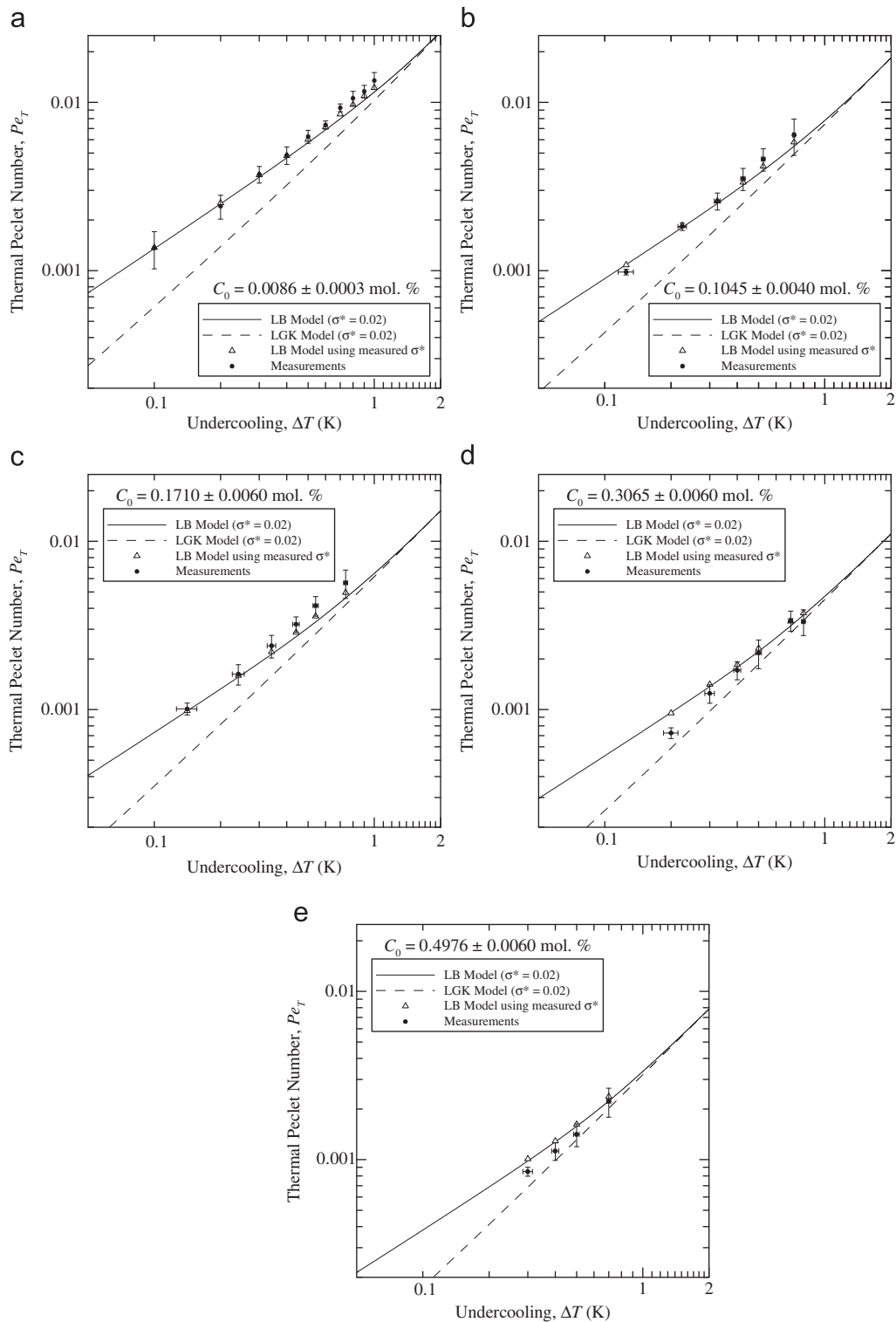
Fig. 10. Comparison of measured and predicted tip growth Péclet numbers as a function of undercooling: $C_0=$ (a) 0.0086, (b) 0.1045, (c) 0.1710, (d) 0.3065, (e) 0.4976 mol%.

in agreement with the present tip shape selection theory for free growth of alloy dendrites, Eq. (20) [1]. The authors are not aware of a previous unambiguous experimental validation of this part of the theory. The alloy data of Chopra et al. [8] exhibit a large scatter of σ^* with C_0 [11]. Since the melt convection in the present experiments depends strongly on the undercooling and the alloy composition, it follows that the selection parameter for alloys is also independent of the convection intensity. This finding is in agreement with the

measurements of Glicksman and coworkers who compared pure substance σ^* data for dendrites grown in microgravity and on earth [28,42].

The fourth-order amplitude coefficients, A_4, measured in the present study for almost pure SCN are plotted in Fig. 13 as a function the undercooling. As discussed in Section 2.3.2, no data are reported here for the more concentrated alloys due to the early onset of sidebranching. Fig. 13 shows that within the
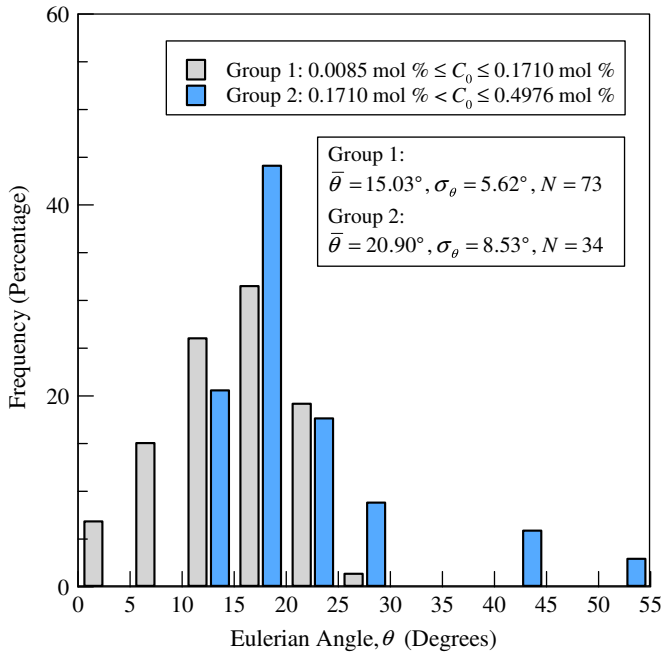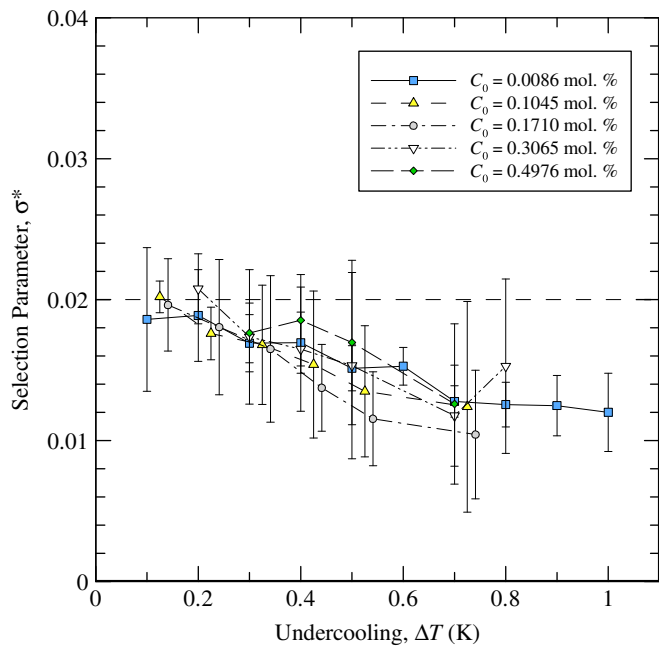
Fig. 11. Histogram of measured Eulerian angles.

Fig. 12. Variation of the measured selection parameter with undercooling for various SCN–acetone alloys.

Fig. 13. Fourth-order amplitude coefficient measured at various undercoolings for almost pure SCN.

measurement uncertainty, the amplitude coefficient is constant and equal to 0.004. This is the same value as determined by Karma et al. [16] using phase–field simulation (dashed line). It is different from the microscopic solvability theory (MST) value of $1/96 = 0.0104$ [43] (solid line), which apparently is in error. Karma et al. [16] obtained good agreement of their prediction of A_4 with the pure SCN dendrite tip shape measurements of LaCombe et al. [15]. However, those measurements were for a single undercooling. A slight decrease of A_4 with increasing undercooling may be inferred from Fig. 13, but such a decrease cannot be confirmed due to experimental uncertainty. It was not possible to measure A_4 to within a reasonable uncertainty for undercoolings greater than 0.6 K, because the dendrite tip becomes too small ($R < 10\ \mu m$).

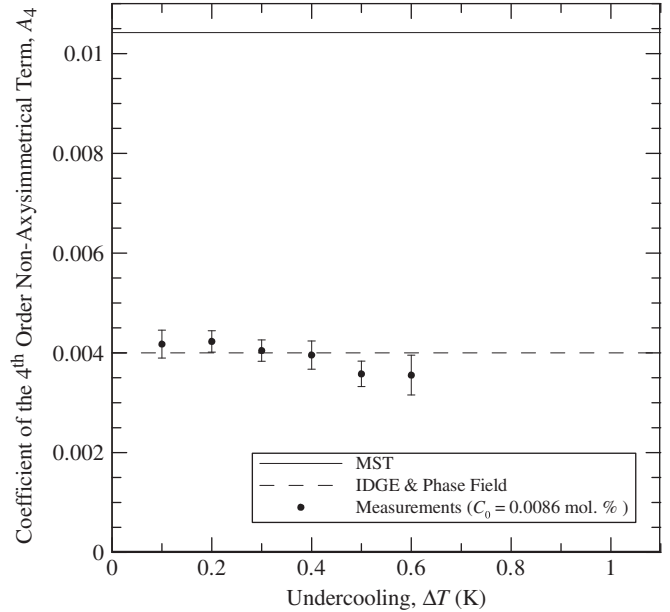### 4.4. Dendrite sidebranch scaling

The sidebranching parameters measured in the present study are shown in Figs. 14–16. In each of these figures, the data for almost pure SCN are plotted in a different graph from those for the more concentrated SCN–acetone alloys. This is necessary because the pure substance and alloy data follow potentially different scaling laws. One reason for such a difference could be that the onset of sidebranching for alloy dendrites occurs closer to the tip than for pure substances. All sidebranching parameters are non-dimensionalized using the measured dendrite tip radius, R, and plotted against the normalized distance from the dendrite tip, z/R. In this way, the data for different experiments, covering a range of initial solute concentrations and undercoolings, can be plotted in a single graph. For distances from the tip of $1 < z/R < 10$, Brener's [33] non-axisymmetric needle crystal solution for the shape of the fins, Eq. (8), is included in each figure. This helps to visualize how a needle crystal evolves into a sidebranching dendrite. The sidebranching measurements start at $z/R = 10$ and extend to about $z/R = 300$. In this range, the present data are fitted to simple power laws (hence, a log–log scale is used in all graphs) and compared to the sidebranch scaling laws obtained previously for pure SCN dendrites grown in microgravity [23,25]. Hence, the effects of convection and of alloy composition can be examined.

The measured sidebranch envelope widths, X_{act}, are plotted in Fig. 14. Excellent scaling can be observed for both the almost pure SCN data (Fig. 14a) as well as for the SCN–acetone alloy data (Fig. 14b). The fit of the almost pure SCN data for $z/R > 10$ is given by

$$\frac{X_{act}}{R} = 0.60\left(\frac{z}{R}\right)^{0.92} \quad \text{(almost pure SCN)} \tag{21}$$

This fit merges smoothly to the needle crystal solution at $z/R = 10$, which is the location of the onset of sidebranching for pure SCN. For pure SCN dendrites grown in microgravity, the pre-factor in the scaling law is given by 0.67 and the exponent by 0.86 [23]. Hence, in the presence of natural convection the sidebranch envelope is wider than in an essentially convection free environment, but the difference is small and becomes significant only for large z/R (see Fig. 14a). The fact that melt convection tends to
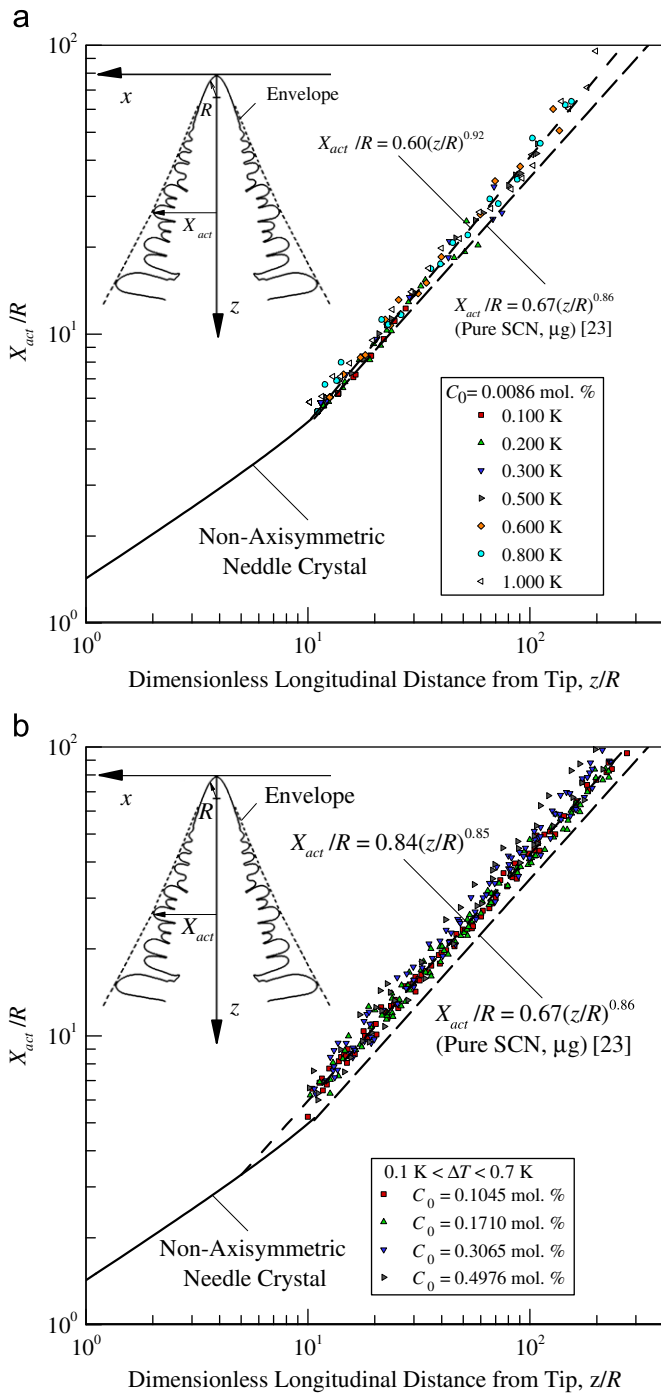
Fig. 14. Measured normalized envelope width (X_{act}/R) as a function of the dimensionless longitudinal distance from the tip (z/R): (a) $C_0 = 0.0086$ mol% (almost pure SCN), (b) 0.1045 mol% $\leq C_0 \leq 0.4976$ mol% (SCN–acetone alloys).

Fig. 15. Measured normalized projection area (F/R^2) as a function of the dimensionless longitudinal distance from the tip (z/R): (a) $C_0 = 0.0086$ mol% (almost pure SCN), (b) 0.1045 mol% $\leq C_0 \leq 0.4976$ mol% (SCN–acetone alloys).

widen the envelope was also observed by Corrigan et al. [24] for pure SCN and by Giummarra et al. [26] for pure PVA. As explained in Section 2.3.3, our envelope measurements cannot be directly compared to this previous data. The fact that convection widens the dendrite envelope can be qualitatively explained as follows. In general, convection tends to increase dendrite tip growth velocities, as already shown by the measurements for the primary tip presented in Fig. 7. The growth direction of the primary tip is approximately aligned with the flow direction, since the flow near the tip is in the direction of gravity. The active sidebranches, however, grow primarily in a horizontal direction, while the melt flow along the sides of the dendrite is still mostly in the vertical direction. As shown by Badillo
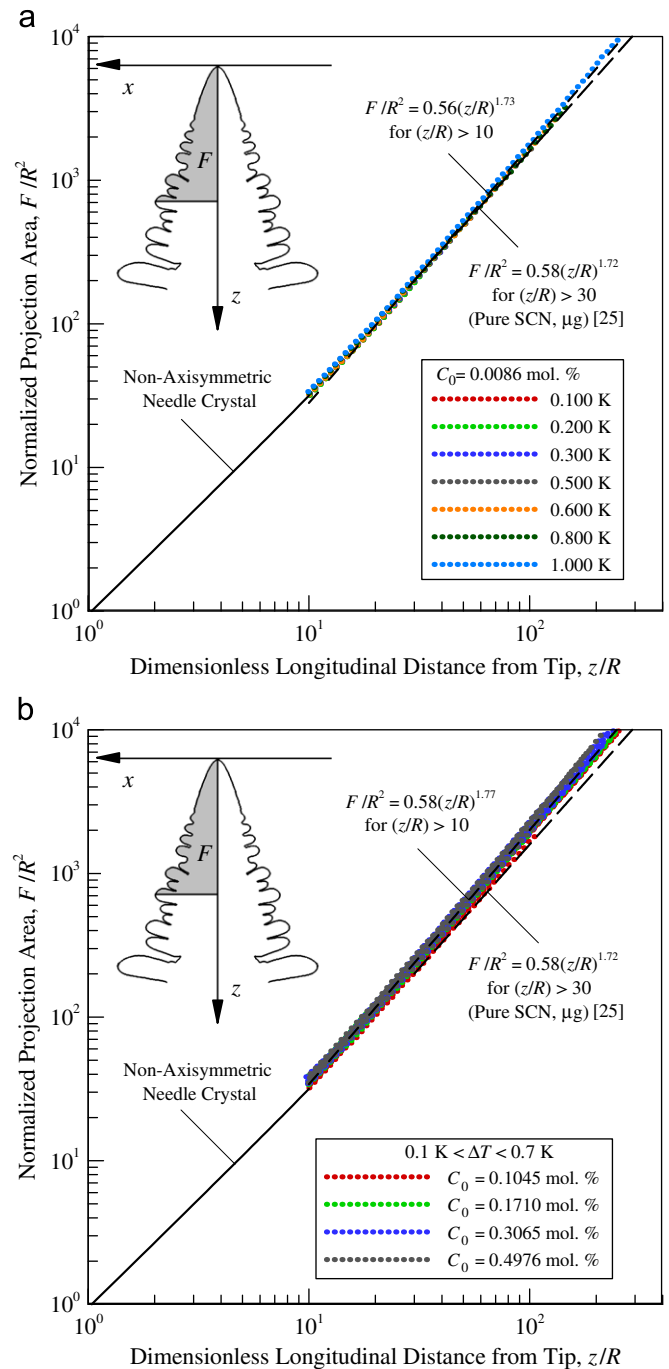
et al. [37], for flow normal to the growth direction, the effect of convection on the dendrite tip velocity is very small. Since the dendrites in the present experiments do not grow exactly downward, and the flow near the active sidebranches is not exactly normal to their growth direction, some enhancement of the sidebranch growth due to convection can still be expected.

The scaling law for the envelope width measured in the present experiments with the four different SCN–acetone alloys is given by

$$\frac{X_{act}}{R} = 0.84 \left(\frac{z}{R}\right)^{0.85} \quad \text{(SCN–acetone alloys)} \tag{22}$$
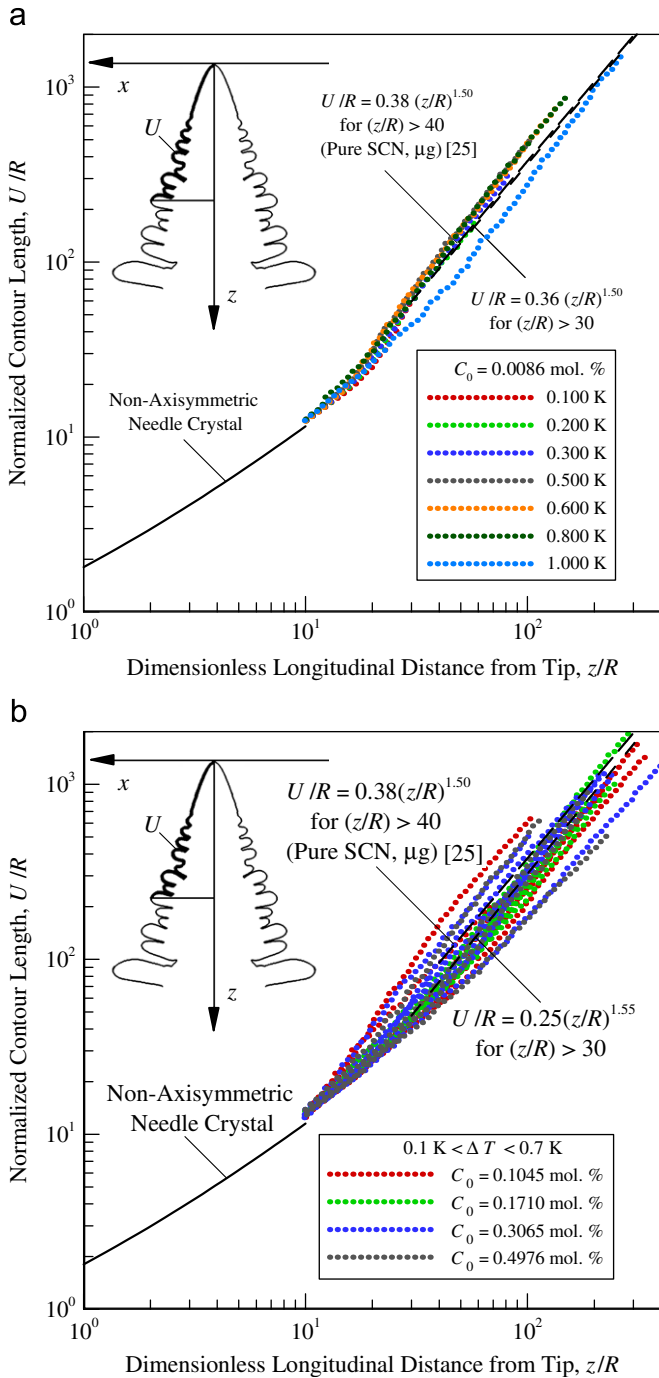
a

b

Fig. 16. Measured normalized contour length (U/R) as a function of the dimensionless longitudinal distance from the tip (z/R): (a) $C_0 = 0.0086$ mol% (almost pure SCN), (b) 0.1045 mol% $\leq C_0 \leq$ 0.4976 mol% (SCN–acetone alloys).

As can be seen from Fig. 14b, this fit merges to the needle crystal solution at $z/R \approx 5$, as opposed to $z/R = 10$ for pure SCN. The difference can be attributed to the earlier onset of side-branching for the alloy dendrites. Also note that the exponent in Eq. (22) is virtually the same as the one in the envelope width scaling law for pure SCN dendrites grown in microgravity [23]. Hence, in Fig. 14b the lines representing the two scaling laws are almost parallel. However, the pre-factor is larger (0.84 compared to 0.67), showing that at any given normalized distance from the tip the envelope of SCN–acetone alloy dendrites is about 25% wider than the one for pure SCN dendrites grown in microgravity. This difference is not due to faster sidebranch tip growth of alloy

dendrites, but simply due to the earlier onset of sidebranching. The effect of convection on the growth of the active sidebranches appears to be small. Comparing Figs. 14a and b, it can be seen that the difference between the two scaling laws given by Eqs. (21) and (22) is significant only for $z/R < 100$. For $z/R > 100$, the normalized envelope widths of almost pure SCN and SCN–acetone alloy dendrites grown on earth are approximately the same (and about 25% larger than those of dendrites grown in microgravity).

The measured dendrite projection areas are plotted in Fig. 15 as a function of distance from the primary tip. Excellent scaling of the data by the primary tip radius can be observed for all undercoolings and alloy concentrations, with the scaling laws given by

$$\frac{F}{R^2} = 0.56\left(\frac{z}{R}\right)^{1.73} \quad \text{(almost pure SCN)} \tag{23}$$

$$\frac{F}{R^2} = 0.58\left(\frac{z}{R}\right)^{1.77} \quad \text{(SCN–acetone alloys)} \tag{24}$$

The difference between these two scaling laws is very small (see Figs. 15a and b), if not negligible, and all data could have been fitted to the same power law. The earlier onset of side-branching for alloy dendrites compared to pure substance dendrites has apparently no effect on the projection area. Recall that Brener's prediction for the projection area of a needle crystal, Eq. (9), was found by Li and Beckermann [25] to hold up to $z/R = 30$, despite the presence of significant sidebranching in the region $10 < z/R < 30$. In other words, in the linear sidebranching regime, the projection area is generally independent of any sidebranching activity. This explains why the present projection area results for almost pure SCN and SCN–acetone alloys can be so similar, despite the difference in the onset of sidebranching. This similarity is then maintained for larger distances from the tip (i.e., $30 < z/R < 300$). The exponent in the above scaling laws for the projection area, Eqs. (23) and (24), is equal to about 1.75. This value is higher than Brener's prediction of 1.6 for the projection area of a non-axisymmetric needle crystal in the plane of the fins [see Eq. (9)], but the difference is not large. Hence, even at very large distances from the tip, a sidebranching dendrite has a projection area that is only marginally higher than that of a needle crystal ($\sim$20% larger at $z/R = 100$; $\sim$40% larger at $z/R = 300$). The effect of melt convection on the projection area can be examined by comparing the scaling laws given by Eqs. (23) and (24) to the one obtained by Li and Beckermann [25] for SCN dendrites grown in microgravity. As shown in Fig. 15, the difference is negligibly small. The pre-factor of 0.58 and the exponent of 1.72 found by Li and Beckermann [25] are, to within measurement uncertainty, the same as the ones in Eqs. (23) and (24). In Ref. [25], the uncertainties in the pre-factor and exponent are stated to be equal to 0.04 and 0.03, respectively. Similar uncertainties are expected here. In summary, the scaled projection area and, thus, the mean width of sidebranching dendrites are given by a single power law, regardless of the undercooling, alloy composition, and convection intensity.

The dendrite contour lengths measured in the sidebranching region are plotted in Fig. 16 as a function of distance from the primary tip. The scaling by the primary tip radius approximately collapses the data to a single line for all undercoolings and alloy concentrations. The scaling laws are given by

$$\frac{U}{R} = 0.36\left(\frac{z}{R}\right)^{1.50} \quad \text{(almost pure SCN)} \tag{25}$$

$$\frac{U}{R} = 0.25\left(\frac{z}{R}\right)^{1.55} \quad \text{(SCN–acetone alloys)} \tag{26}$$

for $z/R > 30$. The uncertainties in the pre-factors and exponents are about 0.05. The scaling law for almost pure SCN, Eq. (25), is virtually identical with the one obtained by Li and Beckermann

[25] for SCN dendrites grown in microgravity. Hence, the effect of convection on the contour length of the sidebranches is negligibly small. Fig. 16b shows that the contour length data for the SCN–acetone alloys fall somewhat below the pure SCN data, but the difference appears to be insignificant. Hence, as with the projection area, the scaled contour length of the sidebranches is approximately given by a single power law, regardless of the undercooling, alloy composition, and convection intensity. As discussed in Ref. [25], the contour length of the sidebranches is the result of a complex interplay of growth and coarsening processes. The present study shows that these processes are of a rather universal nature.

5. Conclusions

The present terrestrial SCN–acetone alloy dendritic growth experiments yield numerous new data that allow for both the validation of existing theories and the generalization of previous scaling laws. It is found that the LGK model [12,13], modified by Li and Beckermann [11] to account for thermosolutal natural convection in the melt, for the operating state of the tip of freely grown alloy dendrites applies well to the present experiments. The comparison of measured and predicted tip growth Péclet numbers shows that some modification of the LB convection model may be needed to better account for the angle between the growth direction and gravity. The single most important finding of the present study is that the tip selection parameter, σ^*, is indeed independent of the solute concentration of the alloy; previous experiments did not conclusively validate this aspect of the theory. However, a relatively strong dependence of σ^* on the undercooling is observed, which points to some deficiency in the LGK model. The fourth-order universal amplitude coefficient for the fins close to the dendrite tip, A_4, is confirmed to be equal to 0.004 over a range of under-coolings, but its unambiguous measurement for alloys is prevented by the early onset of sidebranching.

The present sidebranching measurements reveal that melt convection tends to widen the sidebranch envelope, but this effect becomes apparent only at large distances from the tip. Furthermore the same scaling law for the envelope width is obtained for alloys as for pure substances, except that the alloy envelope at any given distance from the tip is 25% wider than the one for pure substances due to the earlier onset of sidebranching. On the other hand, a single scaling law was found to exist for the projection area of the sidebranch structure, which is directly related to the mean width of a sidebranching dendrite (including all tips and valleys). This scaling law is valid for all solute concentrations (including pure substances), undercoolings, and convection intensities (including microgravity). Similarly, the contour length of the sidebranch structure is, at least approximately, also given by a single scaling law. This indicates that the sidebranch structure of alloy dendrites far from the tip is indeed self-similar and obeys certain universal scaling laws. Previous studies did not establish this fact for alloy dendrites over a range of solute concentrations.

Acknowledgements

References

[1] R. Trivedi, W. Kurz, International Materials Reviews 39 (1994) 49–74.
[2] A. Karma, in: V. Fleury, J.F. Gouyet, M. Léonetti (Eds.), Branching in Nature, Vol. 13, EDP Sciences/Springer-Verlag, Les Houches, 2001, pp. 365–401.
[3] H. Müller-Krumbhaar, W. Kurz, E. Brener, Phase Transformations in Materials, in: G. Kostorz (Ed.), WILEY-VCH Verlag GmbH, Weinheim, 2001, pp. 81–170.
[4] M. Asta, et al., Acta Mater 57 (2009) 941–971.
[5] M. Kahlweit, Journal of Crystal Growth 6 (1970) 125.
[6] S.K. Chan, H.H. Reimer, M. Kahlweit, Journal of Crystal Growth 43 (1978) 229.
[7] A. Dougherty, J.P. Gollub, Physical Review A 38 (1988) 3043–3053.
[8] M.A. Chopra, M.E. Glicksman, N.B. Singh, Metallurgical Transactions 19A (1988) 3087.
[9] M.E. Glicksman, N.B. Singh, M. Chopra, Journal of Crystal Growth 92 (1988) 543.
[10] Ph. Bouissou, B. Perrin, P. Tabeling, Physical Review A 40 (1989) 509.
[11] Q. Li, C. Beckermann, Journal of Crystal Growth 236 (2002) 482–498.
[12] J. Lipton, M.E. Glicksman, W. Kurz, Materials Science and Engineering 65 (1984) 57.
[13] J. Lipton, M.E. Glicksman, W. Kurz, Metallurgical Transactions 18A (1987) 341.
[14] A. Dougherty, M. Lahiri, Journal of Crystal Growth 274 (2005) 233–240.
[15] J.C. LaCombe, M.B. Koss, V.E. Fradkov, M.E. Glicksman, Physical Review E 52 (1995) 2778.
[16] A. Karma, Y. Lee, M. Plapp, Physical Review E 61 (2000) 3996.
[17] A. Dougherty, P.D. Kaplan, J.P. Gollub, Physical Review Letters 58 (1987) 1652–1655.
[18] A. Dougherty, R. Chen, Physical Review A 46 (1992) 4508.
[19] A. Dougherty, A. Gunawardana, Physical Review E 50 (1994) 1349.
[20] E. Hurlimann, R. Trittibach, U. Bisang, J. Bilgram, Physical Review A 46 (1992) 6579.
[21] U. Bisang, J. Bilgram, Physical Review Letters 21 (1995) 3898.
[22] U. Bisang, J. Bilgram, Physical Review E 54 (1996) 5309.
[23] Q. Li, C. Beckermann, Physical Review E 57 (1998) 3176.
[24] D.P. Corrigan, M.B. Koss, J.C. LaCombe, K.D. de Jager, L.A. Tennenhouse, M.E. Glicksman, Physical Review E 60 (1999) 7217–7223.
[25] Q. Li, C. Beckermann, Acta Materialia 47 (1999) 2345.
[26] C. Giummarra, J.C. LaCombe, M.B. Koss, J.E. Frei, A.O. Lupulescu, M.E. Glicksman, Journal of Crystal Growth 274 (2005) 317.
[27] O. Wittwer, J.H. Bilgram, Physical Review E 74 (2006) 041604.
[28] M. Koss, J.C. LaCombe, L. Tennenhouse, M.E. Glicksman, E. Winsa, Metall. Mater, Trans 30A (1999) 3177.
[29] D.L. Ceynar, C. Beckermann, Journal of Crystal Growth 222 (2001) 380–391.
[30] ⟨http://rsb.info.nih.gov/ij/⟩.
[31] N. Draper, H. Smith, Applied Regression Analysis, John Wiley & Sons, New York, 1998.
[32] M. Ben Amar, E. Brener, Physical Review Letters 71 (1993) 589.
[33] E. Brener, Physical Review Letters 71 (1993) 3653.
[34] C.Y. Wang, C. Beckermann, Metallurgical Transactions 24A (1993) 2787–2802.
[35] C.Y. Wang, S. Ahuja, C. Beckermann, H.C. de Groh III, Metallurgical Transactions 26B (1995) 111–119.
[36] I. Steinbach, C. Beckermann, B. Kauerauf, Q. Li, J. Guo, Acta Materialia. 47 (1999) 971–982.
[37] A. Badillo, D.L. Ceynar, C. Beckermann, Journal of Crystal Growth 309 (2007) 197–215.
[38] A. Badillo, D.L. Ceynar, C. Beckermann, Journal of Crystal Growth 309 (2007) 216–224.
[39] P. Delaleau, C. Beckermann, R.H. Mathiesen, L. Arnberg, ISIJ International 50 (2010) 1886–1894.
[40] G. Ivantsov, Doklady Akademii Nauk. SSSR 58 (1947) 567.
[41] B. Cantor, A. Vogel, Journal of Crystal Growth 41 (1977) 109.
[42] J.C. LaCombe, M. Koss, M.E. Glicksman, Metall. Mater, Trans 38A (2007) 116.
[43] E. Brener, V.I. Melnikov, JETP 80 (1995) 341.